2020-9

Gradient-Based Optimization of Solar-Regenerative High-Altitude Long-Endurance Aircraft

Taylor McDonnell
Brigham Young University, taylor.golden.mcdonnell@gmail.com

Andrew Ning
Brigham Young University, aning@byu.edu

Gradient-Based Optimization of Solar-Regenerative High-Altitude Long-Endurance Aircraft

Taylor McDonnell* and Andrew Ning†
Brigham Young University, Provo, UT, 84602, USA

DOI: 10.2514/1.C035566‡.

This paper uses gradient-based optimization to minimize the mass of a solar-regenerative high-altitude long-endurance (SR-HALE) flying-wing aircraft while accounting for nonlinear aeroelastic effects. The aircraft is designed to fly year round at 35° latitude at 18 km above sea level and subjected to energy capture, energy storage, material failure, local buckling, stall, longitudinal stability, and coupled flight and aeroelastic stability constraints. The optimized aircraft has an aspect ratio of 54.52, a surface area of 73.56 m^2, a mass of 349.5 kg, exhibits little aeroelastic deflection at the design airspeed, and is primarily stability constrained. Several parameter sweeps are performed to determine sensitivity to altitude, latitude, battery specific energy, solar efficiency, avionics and payload power requirements, and minimum design velocity.

I. Introduction

A long-envisioned goal in the aerospace community is the development of a solar-regenerative high-altitude long-endurance (SR-HALE) unmanned aerial vehicle (UAV) capable of sustaining year-round flight at high altitudes[1]. SR-HALE UAVs have the potential to provide capabilities similar to satellites in the areas of surveillance, communication, and environmental monitoring at a fraction of the cost [2]. These incentives have led many companies to pursue the development of SR-HALE aircraft (e.g., AeroVironment, Airbus, Boeing, Facebook, and Google) and have, in part, motivated many conceptual designs and/or optimizations on the subject.

Previous SR-HALE aircraft conceptual design and/or optimization studies include those performed by Cestino[3], Baldock and Mokhtarzadeh-Dehghan[4], Nickol et al.[5], Burton and Hoburg[6], Burton et al.[7], and Colas et al[8, 9]. Cestino performed a detailed preliminary design and analysis of a blended wing body SR-HALE configuration[3]. Baldock and Mokhtarzadeh-Dehghan used a simple conceptual design framework to assess the feasibility of a braced wing SR-HALE concept and found year-round SR-HALE aircraft flight to be feasible below 10° latitude[4]. Nickol et al. optimized many high-altitude pseudo-satellite (HAPS) concepts (including SR-HALE aircraft) to find the feasibility of each concept for hurricane science and communications relay missions[5]. While SR-HALE aircraft did not perform well compared to other HAPS concepts in that study (year-round flight was found to be infeasible, even with large technological advances), more recent optimizations have found the SR-HALE concept to be feasible. These studies include those performed by Burton et al.[6, 7] and Colas et al[8, 9]. Burton and Hoburg used geometric programming to perform optimizations of SR-HALE aircraft which took just a few seconds each[6]. The speed of this approach allowed Burton et al. to generate many Pareto fronts which show the sensitivity of SR-HALE aircraft designs to various mission requirements and technological capabilities[7]. Colas et al., on the other hand, presented a more computationally expensive, but higher fidelity SR-HALE aircraft optimization approach in which the flexible aircraft analysis tool ASWING[10] was incorporated into a gradient-free optimization framework[8, 9]. This optimization framework was then demonstrated on single-boom, twin-boom, and flying-wing SR-HALE aircraft.

In all of these studies, optimal SR-HALE aircraft designs tend towards high aspect ratio designs with low structural weight. High aspect ratio wings allow for increased aerodynamic efficiency by reducing induced drag. Lower aircraft mass allows SR-HALE aircraft to conserve energy by flying slower. As a result of these characteristics, SR-HALE aircraft tend to be structurally flexible.

Motivated by the flexibility of SR-HALE aircraft, many researchers have worked towards understanding the impact of extreme aircraft structural flexibility on aircraft performance. Patil and Taylor found that spanwise, non-uniform gusts invoke stronger structural responses in flexible flying wings than uniform gusts[11, 12]. Shearer and Cesnik showed that linearized structural analysis is inappropriate for analyzing the asymmetric maneuvering of flexible aircraft [13]. Su and Cesnik concluded that flutter analyses should consider the whole vehicle's degrees of freedom, and that performing wind tunnel tests in a constrained model may not be sufficient for flexible aircraft flutter

*Ph.D. Candidate, Department of Mechanical Engineering; taylormcd@byu.edu. Student AIAA.
†Associate Professor, Department of Mechanical Engineering; aning@byu.edu. Associate Fellow AIAA.

‡Published in the AIAA Journal of Aircraft. 18 Sep 2020. https://doi.org/10.2514/1.C035566

predictions[14]. Mardanpour et al. found that a non-negligible increase in a flexible aircraft's flutter speed occurs when engines are placed ahead of the wing's elastic axis[15, 16]. Based on many of these findings, Cesnik et al. provided a brief critical review of many conventional structural design procedures applied to very flexible aircraft and provided three recommendations for flexible aircraft design environments[17]. First, the deformed aircraft geometry should be the baseline in weight, structural, and stability analysis. Second, coupling between aeroelasticity and flight dynamics needs to be considered. Third, transient dynamic simulations should include large nonlinear aircraft displacements.

Among the aforementioned studies focused on the conceptual design of SR-HALE aircraft, only those performed by Colas et al[8, 9]. incorporate the flexible aircraft design environment recommendations provided by Cesnik et al[17]. Their approach was to combine a number of existing analysis tools into a gradient-free optimization framework. The advantage of gradient-free optimization is that it places little or no restrictions on the analysis tools which may be used within the optimization. The disadvantage of this approach, however, is that it is computationally expensive compared to gradient-based optimization and geometric programming, especially for large numbers of design variables. Geometric programming, on the other hand, while fast, requires that the objective and constraints are defined using monomials and posynomials. While this restriction allows these problems to be solved incredibly fast, it also makes incorporating higher fidelity models into the optimization framework extremely challenging. The purpose of this paper is therefore to present an SR-HALE aircraft optimization framework which accounts for the peculiarities of structurally flexible aircraft while remaining suitable for use with gradient-based optimization. Using this framework, we also perform several parameter sweeps to determine SR-HALE aircraft design sensitivities to altitude, latitude, battery specific energy, solar panel system efficiency, avionics and payload power, and minimum design velocity.

II. Methods

For demonstrating how gradient-based optimization may be used to optimize SR-HALE aircraft while accounting for the nonlinearities caused by aircraft flexibility, we use a swept flying wing configuration, similar to Facebook's Aquila, as our baseline aircraft configuration. Our objective is to minimize the total aircraft mass as a surrogate for cost. In order to ensure that our optimization framework is appropriate for gradient-based optimization, our objective and constraints will be modeled as continuous and differentiable functions of continuous design variables.

Mission Requirements

The mission of our optimized aircraft is to carry a communication payload year-round at high-altitudes. We design the aircraft to fly 18 km above sea level in order to avoid commercial and military air traffic. Additional motivation for this design altitude is the significant reduction of average wind speeds which occur around 18 km compared to lower altitudes, which reduce station keeping power requirements[18]. We also use the same payload mass and power requirements as used by Colas et al.[8, 9], who assumed a 10 kg payload with a continuous 150 W power draw. We model this payload as a point mass located at the midpoint of the root section chord.

We set the upper bound for the year-round operation of our optimized aircraft at 35° latitude. This allows the aircraft to service more than 74 % of the world's population[19]. Sufficient energy must be captured by solar panels to sustain year-round flight at any location within this latitude band. This requirement is met if the aircraft can collect enough energy to offset its power requirements during any 24 hour period during the year ($E_{\text{in}} \geq E_{\text{out}}$). The most extreme 24 hour scenario within the designated latitude band is winter solstice at 35° latitude, so we use winter solstice operating conditions in this study.

Aircraft Configuration

Since we are designing our optimization framework to work with gradient-based optimizers, discrete design parameters are fixed during our optimizations. These discrete design parameters include, among others, the number of motors/propellers, spanwise break sections, and battery pods. For our optimization, we chose to parameterize our baseline swept flying wing aircraft using six spanwise stations as shown in Fig. 1 with motors, propellers, and battery pods located at stations 3 and 4.

Geometric design variables (which must be continuous) include span b, sweep Λ, chord length $\boldsymbol{c}$, airfoil thickness ratio $\boldsymbol{t/c}$, twist $\boldsymbol{\theta}$, winglet length l_{winglet}, and winglet dihedral ψ_{winglet}. We measure sweep from the leading edge of each airfoil section, chord lengths in the streamwise direction, and twist normal to the swept wing. We specify chord length, twist, and airfoil thickness ratios at each of the six stations and linearly interpolate these parameters between stations. To accommodate the aircraft payload, we constrain the root chord length to be greater than or equal to that of the baseline Aquila configuration $c_{\text{root}} \geq 2\,\text{m}$. With the wing defined by six spanwise stations, these geometric design variables account for 22 of the 44 design variables used in our optimization.

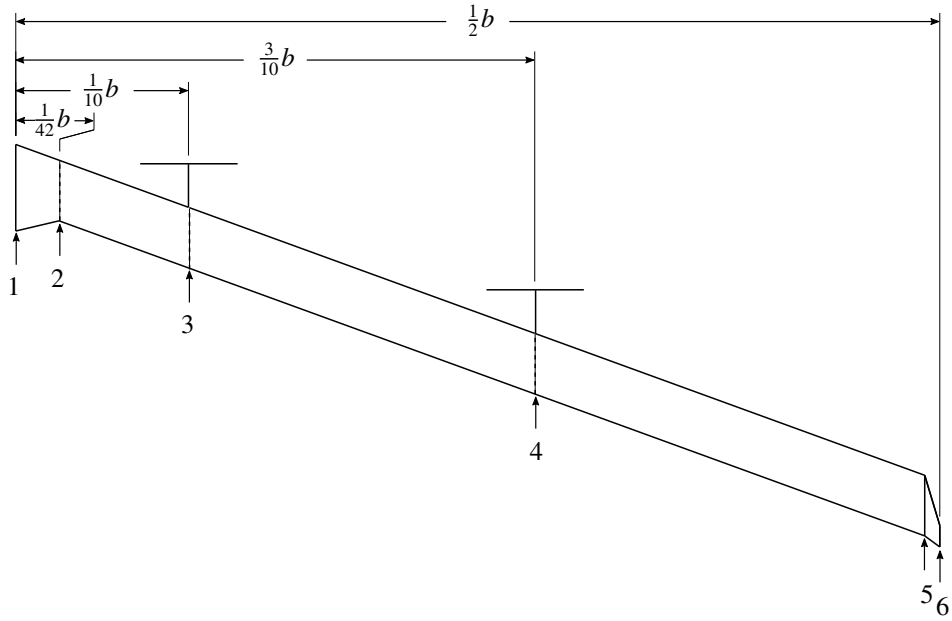

Figure 1: The parameterized baseline configuration for this study, defined at six spanwise stations.

While we design the aircraft to be trimmed without flap deflections during design operation ($\sum F = 0.0$ and $\sum M = 0.0$), flaps are added to the aircraft between stations 4 and 5 to allow for off-design trimmed-flight operating point evaluation and active control during gust simulations. The flap derivatives we use in this study are presented in Table 1. These flap derivatives were chosen based on flap deflection calculations using XFOIL at a Reynolds number of 4×10^5 with the E216 airfoil.

Table 1: Assumed aileron flap derivatives

$dc_l/d\delta_f$	$0.08/^\circ$
$dc_d/d\delta_f$	$0.001/^\circ$
$dc_m/d\delta_f$	$-0.01/^\circ$

Aircraft Structure

Discrete structural design choices which are fixed for the duration of the optimization include the choice of the wing's structural layout (I-beam, box beam, or stiffened skin) and the number, material, and organization of the plies in the structure. For our optimization we chose to use a box beam and stiffened skin configuration, as shown in Fig. 2. We use high modulus carbon fiber reinforced polymer (CFRP) as our primary SR-HALE aircraft structural material due to the stability-constrained nature of flying wing SR-HALE aircraft[9, 20]. Material properties are given in Tables 2 and 3. Both the stiffened skin and the box beam layups feature a sandwich structure in order to increase the bending stiffness of limited numbers of CFRP plies. Balanced and symmetric layups are used to minimize membrane/bending and stretching/shearing coupling, respectively[21]. CFRP fabric is placed on the outside of the aircraft to reduce impact damage and provide torsional rigidity. Unidirectional CFRP is aligned with the axial direction to increase bending stiffness.

Table 2: Assumed Material Stiffness Properties

Material	E_1 (GPa)	E_2 (GPa)	G_{12} (GPa)	ν_{12}	ρ (kg/m^2)	t_{ply} (mm)
High Modulus CFRP Tape	175.0	8.0	5.0	0.30	1600	≥ 0.1
High Modulus CFRP Fabric	85.0	85.0	5.0	0.10	1600	0.1
Foam	0.048	0.048	0.028	0.3	75.0	≥ 1

The structural design variables we use in our optimization are spar cap location $(x/c)_{spar}$, measured from the

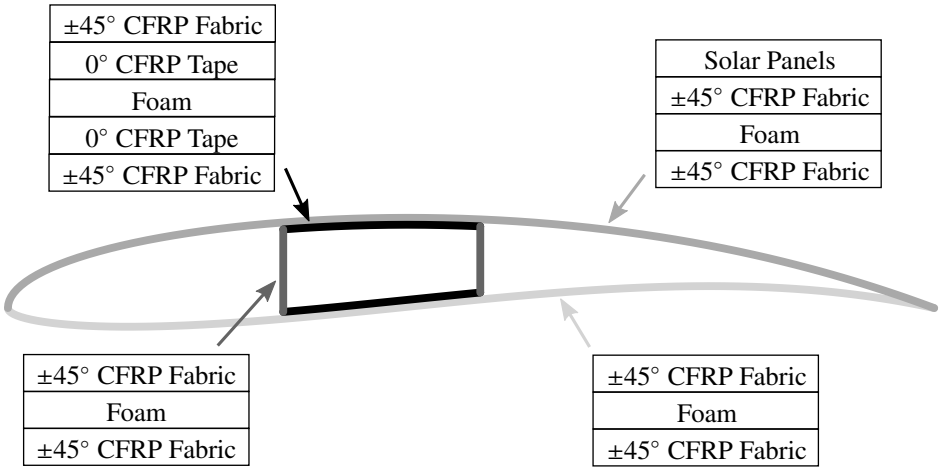

Figure 2: Box beam and stiffened skin configuration assumed in this study.

Table 3: Assumed Material Strength Properties

Material	S_1^+ (MPa)	S_1^- (MPa)	S_2^+ (MPa)	S_2^- (MPa)	S_{12} (MPa)
High Modulus CFRP Tape	1000.0	850.0	40.0	200.0	60.0
High Modulus CFRP Fabric	350.0	150.0	350.0	150.0	35.0

leading edge to the center of the spar and normalized by the section chord length, foam core thicknesses in the skin $t_{\text{foam,skin}}$ and in the webs $t_{\text{foam,web}}$, spar cap ply thicknesses $\boldsymbol{t}_{\text{spar}}$, and spar cap widths ($\boldsymbol{w}_{\text{spar}}$. We constrain foam core thicknesses to be greater than 1 mm to prevent optimal designs with unrealistically small foam core thicknesses. Spar cap ply thicknesses are similarly constrained to be greater than the thickness of a single ply, which we assume in this study to be 0.1 mm.

Physically, spar cap thicknesses cannot be varied continuously, but are rather discrete, often-fixed design parameters. We have, however, included spar cap thicknesses as design variables in this optimization in order to approximate adding additional plies to the spar cap in a manner appropriate for gradient-based optimization. These thicknesses, as well as spar cap widths, are linearly interpolated between stations.

Airfoil Shape and Performance

While ideally an aerodynamic analysis of arbitrary airfoil shapes would be performed within the optimization, such an analysis has the potential to be computationally expensive since it must be performed for each combination of airfoil shape and flow conditions. We therefore decided to precompute two-dimensional lift, friction drag, profile drag, and moment coefficients for a range of airfoil thickness-to-chord ratios, Reynolds numbers, and angles of attack using XFOIL[22]. These values were then fit with three dimensional cubic-splines which are used in the optimization. We then inspected the splines manually for agreement with the XFOIL data. The airfoil we used for these calculations was the E216 airfoil. We chose this airfoil because it is a low-Reynolds number airfoil with gradual stall characteristics and a large drag bucket (as predicted by XFOIL at its original thickness). A depiction of this airfoil with varying thicknesses is shown in Fig. 3. A slice of two of the resulting three dimensional splines at a Reynolds number of 4×10^5, is shown in Figs. 4a and 4b.

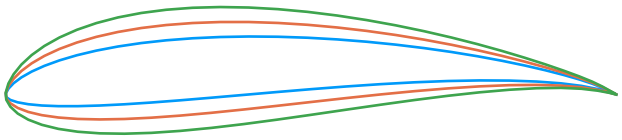

Figure 3: Selected airfoils from the airfoil family used in this study, generated by modifying the thickness of the E216 airfoil

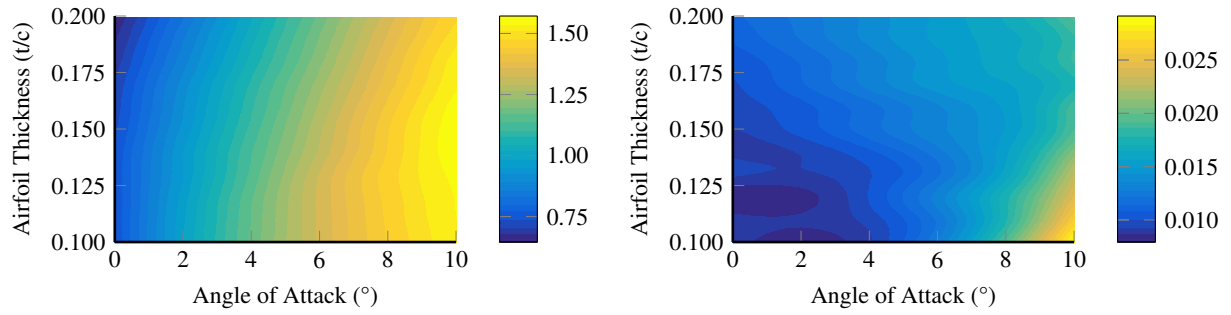

(a) Lift Coefficient

(b) Drag Coefficient

Figure 4: E216 airfoil family lift and drag coefficient variation with thickness and angle of attack at a Reynolds number of 4×10^5.

Propulsion System

To reduce computational expense and simplify the propeller analysis, we assume that the propeller's performance can be represented using the non-dimensional torque, thrust, and efficiency curves shown in Figs. 5a to 5c. We calculated these propeller performance curves using blade element momentum theory in a coupled SR-HALE trajectory and propulsion optimization study[23]. While the majority of the propeller design remains fixed for the course of the optimization, propeller size and rotation rate are set by the optimizer through its choice of propeller diameter (D_p) and advance ratio (J).

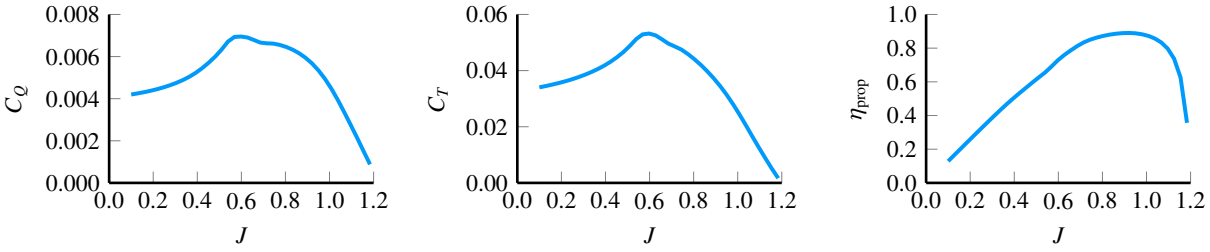

(a) Torque Coefficient

(b) Thrust Coefficient

(c) Efficiency

Figure 5: Assumed propeller non-dimensional properties

We estimate motor performance using the same first-order, steady-state, brushed, direct current motor model used by Drela in QPROP[24]. We use propeller torque and rotation rate as inputs to the motor model to couple the motor and propeller dynamics. We also assume that the relationship between no load current I_0 and internal resistance is given by the following empirical expression, which was constructed using AstroFlight motor data[25]:

$$R = 0.0467 I_0^{-1.892}$$

The design variables we use to design the motors are no-load current I_0 and motor speed constant K_v. We set bound constraints on these design variables so that they are within the range of data used for the empirical curve fit ($32 \leq K_v \leq 1355$ and $0.1 \leq I_0 \leq 6.0$). We have not incorporated a weight model for the motor and propeller into the optimization but rather model each motor and propeller combination as a 5 kg point mass located one meter in front of the aircraft at stations 3 and 4, as shown in Fig. 1.

Power Requirements

Total power required is given by:

$$P_{\text{req}} = \frac{V_\infty D}{\eta_{\text{motor}} \eta_{\text{prop}} \eta_{\text{other}}} + P_{\text{avionics}} + P_{\text{payload}}$$

where V_∞ is the freestream velocity, D is the total aircraft drag, η_{motor} is the motor efficiency, η_{prop} is the propeller efficiency, η_{other} is the efficiency of all other components of the propulsion system (assumed in this study to be 0.97), P_{avionics} is the power required by the avionics system, and P_{payload} is the power required by the payload. We assume the avionics and payload combined require 400 W of continuous power.

Battery Mass

Reported cell specific energies on Airbus's Zephyr have specific energies of 435 Whr/kg[a]. After accounting for additional mass due to battery packaging, lower specific energies can be expected. We therefore set battery specific energy equal to 350 Whr/kg. Additionally, since batteries degrade rapidly when allowed to fully discharge, we limit battery depth of discharge to 80 %, effectively limiting battery specific energy to 280 Whr/kg. Batteries are modeled as four point masses located at stations 3 and 4 (the same spanwise locations as the motors and propellers). The normalized chord-wise location of these point masses is fixed at the quarter chord of their respective airfoil section chord lines. Inboard and outboard battery masses ($m_{\text{batt,in}}$, $m_{\text{batt,out}}$) may vary subject to the restriction that total available energy storage be greater than the energy required for night-long flight ($m_{\text{batt,total}} \geq m_{\text{batt,req}}$).

Energy Capture

Energy capture is provided by solar panels covering the aircraft's upper surface. We assume that solar panels have the same thickness as those used on the Solar Impulse (135 µm)[b]. Available solar flux is determined through using the Simple Model of the Atmospheric Radiative Transfer of Sunshine (SMARTS)[26]. The aircraft starts the day facing northward and follows a steady level 3 km radius counterclockwise orbit throughout a 24-hour period. The roll necessary to maintain this orbit is determined by that of a coordinated turn:

$$\phi = \tan^{-1}\left(\frac{V^2}{gR}\right)$$

where V is cruise velocity, g is gravity, and R is the orbit radius. The yaw angle is determined by assuming the aircraft is always oriented tangent to the orbit radius.

To determine the total amount of solar capture on the upper surface of the aircraft, the aircraft is discretized spanwise and chordwise into flat panels with associated roll, pitch, yaw, and area. This discretization is performed using the shape of the aircraft at the design operating point. Panel normal vectors are compared with sun vectors throughout the day (using the dot product) to determine the incident solar flux on each panel at each time step. For the cases where the sun is located behind the solar panels, the incident solar flux is clipped at zero using a smooth approximation of the maximum function, the Kreisselmeier-Steinhauser function[27] (which is discussed later in this paper), so that the resulting expression for energy capture remains continuous and differentiable. This flux is numerically integrated across the 24 hour period and multiplied by panel area to determine the amount of solar energy captured by each panel. This energy capture is then reduced using a total solar panel system efficiency of 20 %. The Solar Impulse used 23 % efficient solar panels, so in comparison, the solar panel system efficiency we use in this paper is conservative.

Flight Envelope

We chose to use select transport aircraft design regulations as a basis for the structural sizing of the SR-HALE aircraft considered in this study. We expect this practice to result in the development of conservative SR-HALE aircraft designs. Following this approach, we set the dive speed to 125 % of the design cruise speed and the flutter speed to 110 % of the dive speed. Additionally, structural integrity is required at load factors ranging from −1.0 to 2.5. For the aircraft's flight envelope, we chose to set the maximum cruise equivalent airspeed (EAS) 5 m/s above the design airspeed to provide a sufficient buffer for trajectory optimization and/or other maneuvering at altitude. The resulting flight envelope is shown in Fig. 6.

Lettered operating points on Fig. 6 correspond to quasi-steady operating point evaluation locations where we constrain the aircraft against material failure and local buckling with a safety factor of 1.5. Numbered operating points correspond to flutter evaluation locations, where we constrain the aircraft against failure due to aerostructural instabilities as well as material failure and local buckling. For operating points (except at the design airspeed, which is designed to be trimmed) we vary angle of attack to achieve the specified load factor. For flutter evaluation locations we

[a]Data available online at `https://aviationweek.com/business-aviation/amprius-developing-more-applications-its-lithium-ion-cells` [retrieved 17 August 2020].

[b]Data available online at `https://aroundtheworld.solarimpulse.com/adventure` [retrieved 17 August 2020].

additionally use elevon deflections to trim the aircraft. Elevons are not used at any other operating point. All structural constraints are evaluated at the design altitude.

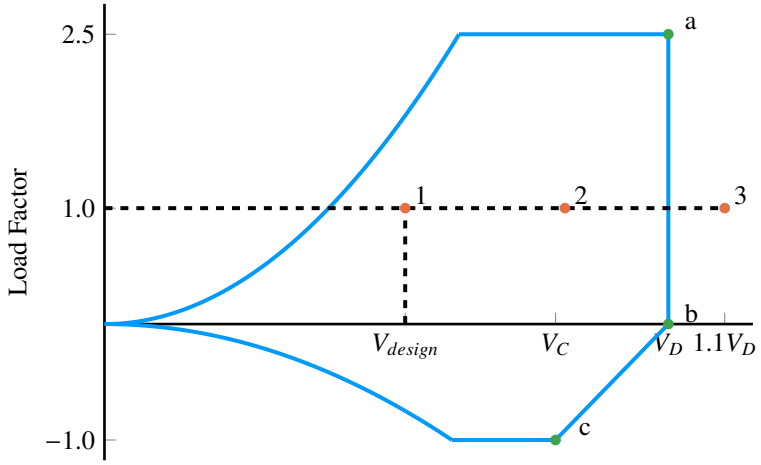

Figure 6: Flight envelope of SR-HALE aircraft in this study.

Non-Uniform Gust Encounters

Flexible flying wing aircraft react more strongly to non-uniform gusts than uniform gusts[11, 12], so we chose to consider only non-uniform gusts. To define our gust profile we decided to use the gust profile defined for transport aircraft in Advisory Circular (AC) 25.341-1, given by:

$$U(x) = \frac{U_{ds}}{2}\left(1 - \cos\frac{\pi x}{H}\right)$$

where U_{ds} is the design gust velocity and H is the gust gradient distance. We modify this gust profile to be non-uniform across the span of the aircraft using the following function:

$$U(x, y) = U(x)\cos\left(\frac{2\pi y}{b}\right)$$

where b is the aircraft span.

We perform three time-domain gust simulations for each optimization iteration using the parameters given in Table 4. We chose these parameters by applying the recommendations of AC 25.341-1 at the design altitude. In all cases, the aircraft's initial state is that of the design operating airspeed, and elevon and throttle inputs are used to restore the aircraft to steady-level flight. Elevon inputs are chosen using a PID control law based on the aircraft's pitch rate. Throttle inputs are chosen through a proportional control law based on the aircraft airspeed. These gains were tuned manually with the initial aircraft design and then fixed for the duration of the optimization, and are presented in Table 5. Material failure and local buckling are constrained throughout the aircraft at each time step of the simulation.

Table 4: Gust Parameters

	U_{ds} (m/s, EAS)	H (meter)
Short Gust	3.712	9.1
Medium Gust	5.053	57.9
Long Gust	5.595	106.7

Flexible Aircraft Aeroelastics

We use ASWING to evaluate the aircraft's aerostructural performance at each of the structural operating points as well as for gust encounters. The main approach of ASWING is to model aircraft as interconnected nonlinear beams with lifting surface properties calculated using extended lifting line theory. Section structural properties are determined

Table 5: Control law gains for gust simulations

$k_{p,\text{pitch rate}}$	-0.4 ° s
$k_{i,\text{pitch rate}}$	-0.02 °
$k_{d,\text{pitch rate}}$	-0.1 °/s^2
$k_{p,\text{throttle}}$	-50.0 N s/m

using PreComp[28], whereas 2D aerodynamic parameters are calculated using XFOIL as previously described. Rather than using a fixed lift curve slope for each airfoil section, we chose to calculate lift curve slopes and airfoil zero lift angle of attacks using local airfoil angle of attack, lift coefficient, and lift curve slope. We use normal twist for the local angle of attack, and get lift coefficient and lift curve slope from the precomputed E216 family splines discussed previously.

We made several changes to the original program in order to make it suitable for gradient-based optimization. We modified the ASWING code so that the number of nodes between each station remained constant, because otherwise discontinuities would have been introduced into the design space due to differing discretizations for each design iteration. We also tightened convergence tolerances in the Newton solution procedure so that gradients could be accurately computed. We removed the eigenvalue post-processing in ASWING as well, to ensure that the number of returned eigenvalues did not change between design iterations. We also stripped the code of a number of print statements and plotting functions. Finally, we developed a wrapper to expose the internals of the program so that we could call and access its various elements directly[c]. For internal use we also developed a fully translated version of ASWING in the Julia programming language so that we could make use of Julia's automatic differentiation capabilities provided by the ForwardDiff package[29]. We use the fully translated version of ASWING in this paper so we could provide exact derivatives to our optimizer.

Material Failure

We calculate axial strain in the same manner as performed by ASWING, except extend ASWING's capabilities to allow axial strain to be calculated at multiple locations along the surface and in the webs of each spanwise section. We compute torsional shear stress in the same manner as performed in CoBlade[30], but use the torsion moment about the shear center computed by ASWING. We then use classical laminate theory to determine ply stresses and strains based on laminate axial strain and torsional shear stress following the approach used in CoBlade. Once we obtain ply stresses and strains, we use first-ply failure as our material failure criteria with failure predicted by Tsai-Wu failure theory[31]. To ensure that the constraint functions we construct using these analyses are smooth we avoided using discontinuous functions (such as the maximum or minimum function) when developing these analyses.

Before using Tsai-Wu failure theory, we apply material scatter and barely visible impact damage (BVID) knockdown factors to CFRP material strengths. We chose material scatter knockdown factors for CFRP tape and fabric based on A-basis values from the Advanced General Aviation Transport Experiments for TORAY T700GC-12K-31E/#2510 Unidirectional Tape and TORAY T700SC-12K-50C/#2510 Plain Weave Fabric[32, 33]. These material scatter knockdown factors are tabulated in Table 6. The impact of barely visible impact damage varies depending on the specific layup used and is typically determined through testing. For this paper, we chose the BVID knockdown factor to be 0.65 which approximately corresponds to a 25 mm impact damage diameter[34].

Table 6: Material Scatter Knockdown Factors

Material	k_1^+	k_1^-	k_2^+	k_2^-	k_{12}
CFRP tape	0.625	0.762	0.803	1.0	0.920
CFRP fabric	0.764	0.776	0.719	0.859	1.0

Local Buckling

For local buckling calculations, we divide the upper and lower surfaces of each airfoil section into several flat panels using the section's webs as shown in Fig. 7. For long simply supported plates, the local buckling load in compression

[c]The code for this wrapper can be found at `https://github.com/byuflowlab/Aswing.jl`

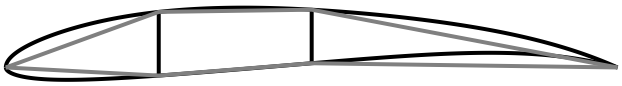

Figure 7: Airfoil section divided up into several flat buckling panels by the section's webs

is:

$$N_{x,cr} = 2\left(\frac{\pi}{b}\right)^2 \sqrt{D_{11}D_{22}} + D_{12} + 2D_{66}$$

and the local buckling load in shear is:

$$N_{xy,cr} = 52K_2 D_{11}/b^2$$

$$K_2 = (D_{22}(D_{12} + 2D_{66}))^{1/2} f(c)/D_{11}$$

$$c = (D_{11}D_{22})^{1/2}/(D_{12} + 2D_{66})$$

$$f(c) = \begin{cases} c^{1/2}(0.62 + 0.38/c), & c \geq 1 \\ 0.89 + 0.04c + 0.07c^2, & c < 1 \end{cases}$$

where b is the panel width[35]. In our optimization framework we use a smooth approximation for $f(c)$ so that the buckling constraint functions are smooth. This smooth approximation is given by:

$$\bar{f}(c) = \frac{1 - \tanh(k(c-1))}{2}(f_1(c) - f_2(c)) + f_2(c)$$

where

$$f_1(c) = c^{1/2}(0.62 + 0.38/c)$$

$$f_2(c) = 0.89 + 0.04c + 0.07c^2$$

and k is a parameter which sets the "hardness" of the transition between the two functions, which we set to 20. These buckling loads together define the upper bound for loads experienced on the surface of the airfoil, with failure due to local buckling occurring when

$$\frac{N_{xy}^2}{N_{xy,cr}^2} + \frac{N_x}{N_{x,cr}} \geq 1$$

at any point along the surface.

The aircraft's webs may experience bending as well as compression and shear. For long simply supported plates, the critical buckling load in bending[36] is

$$N_{xb,cr} = \frac{4}{b^2}\left(13.4\sqrt{D_{11}D_{22}} + 10.4(D_{12} + 2D_{66})\right)$$

We assume failure due to local buckling in the webs occurs when:

$$\frac{N_{xy}^2}{N_{xy,cr}^2} + \frac{N_{xy}^2}{N_{xy,cr}^2} + \frac{N_{xb}}{N_{xb,cr}} \geq 1$$

We constrain local buckling for each web at multiple spanwise locations. For these calculations, N_x is calculated by averaging the loads experienced in the web and N_{xb} is calculated by averaging the load at the top and bottom of the webs and subtracting N_x.

Aircraft Stall

We use critical section theory to constrain aircraft stall ($c_{l,\min} \leq c_l \leq c_{l,\max}$) during design operation. According to critical section theory, a wing stalls when any airfoil section lift coefficient exceeds the corresponding section's maximum or minimum lift coefficient. To provide a buffer against stall during design operation, maximum or minimum lift coefficients are reduced by 90 % on the inboard portion of the wing and up to 80 % on the outboard portions of the wing as defined by the following factor:

$$G(y/b) = \begin{cases} 0.9 & 0 \leq |y/b| \leq 0.25 \\ 0.9 - 1.6(|y/b| - 0.25)^2 & 0.25 < |y/b| \leq 0.5 \end{cases}$$

We reduce maximum and minimum lift coefficients on outboard portions of the wing further than inboard lift coefficients in order to prevent tip stall. We use a smooth stall reduction factor curve in order to ensure that results are continuous and differentiable.

General Stability/Flutter

ASWING can be used to determine coupled flight and aerostructural stability through eigenmode analysis about quasi-steady states. We use this feature of the program in the optimization to assess aircraft stability for airspeeds up to 110 % of the aircraft dive speed. The aircraft configuration is stable for a given set of operating conditions when all eigenvalues are in the left half of the complex plane. Equivalently, the aircraft configuration is stable for a given set of operating conditions when the maximum real part of all eigenvalues is negative. We use the latter constraint formulation, in which the maximum real part of all eigenvalues is constrained to be negative. However, since the maximum function is not smooth, we approximate it using the Kreisselmeier-Steinhauser (KS) constraint aggregation function[27]. This function has the following form:

$$KS(\boldsymbol{g}(\boldsymbol{x})) = \frac{1}{\rho} \ln \left[\sum_{j=1}^{n_g} e^{\rho \boldsymbol{g}_j(x)} \right]$$

where $\boldsymbol{g}(\boldsymbol{x})$ defines a vector of constraint functions, n_g is the length of that vector, and ρ is a parameter that controls the "hardness" of the function. As ρ approaches ∞, the "hardness" of this function increases until $\rho = \infty$ when the actual maximum is returned. A salient feature of this function is that it overestimates the maximum ($KS(\boldsymbol{g}(\boldsymbol{x})) \geq \max(\boldsymbol{g}(\boldsymbol{x}))$) which makes it particularly well suited for the aggregation of constraints since it guarantees a conservative constraint formulation.

To decrease computational expense, only a subset of eigenvalues corresponding to the least stable modes for each considered flight condition are computed using Arnoldi iteration. Fortunately, this approach still allows for a smooth constraint formulation when used with the KS constraint aggregation function, because as the stability of an eigenvalue increases relative to other eigenvalues its influence on the stability constraint decreases rapidly until it can be safely ignored without creating discontinuities in the stability constraint formulation. As a byproduct of this feature of the KS function, regions of the complex plane may be ignored through artificially increasing the stability of these modes. We use this technique in this paper to reduce the impact of eigenvalues with unrealistically high frequency components ($\mathrm{Im}(\lambda) > 20\,\mathrm{Hz}$) and neglect low magnitude eigenvalues ($|\lambda| < 1.0$), which correspond to modes which may be easily controlled using active control methods.

A common approach to choose the parameter ρ is to start with $\rho = 50$, and then decrease ρ as necessary to yield good numerical handling. The maximum relative error between the maximum function and the KS function increases both as ρ is increased and as the number of aggregated values increases. When applied to 100 values with $\rho = 50$ the KS function yields a maximum relative error of 10 % compared to the maximum function. For this study, using $\rho = 50$ results in an infeasible optimization problem, due to the error introduced by the KS function. We therefore chose to use the adaptive approach proposed by Poon and Martins to set the value of ρ when the KS function is used in this optimization[37]

Longitudinal Stability

In addition to the general stability constraint, we constrain the aircraft's static margin to be at least 5 % at the design airspeed (static margin $\geq 5\%$). This constraint is necessary to ensure static longitudinal stability since we neglect low magnitude eigenvalues in our general stability constraint. We set the minimum static margin to 5 % rather than 0 to reduce the amount of control effort that is necessary to maintain the aircraft in steady level flight.

This static margin constraint is enforced through an equivalent constraint on dC_M/dC_L about the aircraft's center of gravity. Traditional stability derivatives are based on rigid aircraft assumptions, however, static margin may still be calculated either by assuming quasi-steady aeroelastic loads or by assuming a rigid aircraft shape (after taking into account deformations due to design operating conditions). We constrain both quasi-steady and rigid aircraft static margin values at each design iteration.

Additional Mass and Drag

We add a mass and drag markup at each design iteration to account for the additional mass and drag of components which are not explicitly modeled. Components which add to aircraft mass which are not explicitly modeled include but are not limited to: avionics, maximum power point tracker, and landing gear mass. Additional drag could result from surface roughness, landing gear drag, and/or protuberance drag. We assume that these miscellaneous factors account for 15 % of the aircraft's mass and 10 % of the aircraft's drag. We apply the mass markup factor to all components which contribute to the aircraft's mass, so that the additional mass is distributed throughout the aircraft.

Optimization Problem

Fully assembled, the optimization problem can be represented as:

minimize:	m_{total}	
with respect to:	$b,\ \Lambda,\ \boldsymbol{c},\ \boldsymbol{t/c},\ \boldsymbol{\theta},\ l_{\text{winglet}},\ \psi_{\text{winglet}},\ t_{\text{foam,skin}},\ t_{\text{foam,web}},\ (x/c)_{\text{spar}},\ \boldsymbol{t}_{\text{spar}},\ \boldsymbol{w}_{\text{spar}},\ V_\infty,$ $m_{\text{batt,in}},\ m_{\text{batt,out}},\ D_p,\ J,\ K_v,\ I_0$	
subject to:	$E_{\text{in}} \geq E_{\text{out}}$	(energy balance constraint)
	$m_{\text{batt,total}} \geq m_{\text{batt,req}}$	(energy storage constraint)
	$c_{\text{root}} \geq 2$ m	(payload storage constraint)
	Tsai-Wu criterion ≤ 1	(material failure constraints)
	$\frac{N_{xy}^2}{N_{xy,cr}^2} + \frac{N_{xy}^2}{N_{xy,cr}^2} + \frac{N_{xb}}{N_{xb,cr}} \leq 1$	(local buckling constraints)
	$c_{l,min} \leq c_l \leq c_{l,max}$	(stall constraints)
	static margin $\geq 5\%$	(static margin constraints)
	$KS(\text{real}(\boldsymbol{\lambda})) \leq 0.0$	(general stability constraints)
	$\sum F = 0.0$	(force trim constraints)
	$\sum M = 0.0$	(moment trim constraints)

In total, the optimization problem involves 44 design variables and over a million constraints. The majority of these constraints are material failure and local buckling constraints from gust simulations, since material failure and buckling constraints are applied throughout the aircraft at each time step. To reduce the computational expense of running the optimization, we chose to reduce the number of material failure and local buckling constraints from gust simulations by aggregating them using the KS constraint aggregation function. After aggregating the gust constraints, the number of constraints reduced to 29,034 constraints.

Verification

Validation and/or verification for pre-existing codes that were used in this optimization, including XFOIL, PreComp, ASWING, and SMARTS, have been performed elsewhere in the literature and/or by the creators of the respective codes[38, 39]. To ensure that these verifications were applicable to our translated versions of PreComp and ASWING we implemented unit tests to ensure that the outputs of the the translated codes matched with the original codes. All spanwise stiffness and inertial properties computed by our translated version of PreComp matched those computed by the original program for the test case provided with the software. Similarly, we were able to match aerodynamic and structural variables, as well as system eigenvalues in our translated version of ASWING to those computed by the original program. For solar capture calculations, we compared the solar flux of the initial aircraft configuration to that of a equivalent flat plate as predicted by SMARTS during winter solstice. We also verified our implementation of classical laminate theory with textbook examples given by Kollár[40].

Sensitivity Analysis

We calculate objective and constraint function sensitivities using forward-mode automatic differentiation, as implemented by ForwardDiff[29], throughout the majority of our code. We use forward-mode rather than reverse-mode automatic differentiation because the number of constraints (29,034) is much larger than the number of design variables (44). In order for our code to be compatible with ForwardDiff we used the Julia programming language to model our optimization problem. Using the Julia language also allows our code to take advantage of significant compiler optimizations, which drastically decreases the computational expense of running our code compared to a Python and/or MATLAB implementation.

We augment the automatic differentiation process with analytic gradients when using Newton's method in ASWING and when calculating eigenvalues. We apply the analytic sensitivity equations around the Newton solver in order to avoid propagating dual numbers through the Newton iterations. For eigenvalue calculations we use analytic gradients rather than automatic differentiation in order to be able to use ARPACK, which is collection of eigenvalue routines written in Fortran (analytic gradients are needed since ForwardDiff automatic differentiation only works with code written in Julia).

The analytical sensitivity equations for the Newton solver take the folowing form:

$$\frac{d\boldsymbol{y}}{d\boldsymbol{x}} = -\left(\frac{\partial \boldsymbol{g}}{\partial \boldsymbol{y}}\right)^{-1} \frac{\partial \boldsymbol{g}}{\partial \boldsymbol{x}}$$

where $\boldsymbol{x}$ is a vector of design variables, $\boldsymbol{y}$ is a vector of state variables, and $\boldsymbol{g}$ is the residual function, which is a function of $\boldsymbol{x}$ and $\boldsymbol{y}$. We re-use $\frac{\partial \boldsymbol{g}}{\partial \boldsymbol{y}}$ since it is already used by Newton's method and calculate $\frac{\partial \boldsymbol{g}}{\partial \boldsymbol{x}}$ using automatic differentiation. After solving for $\frac{d\boldsymbol{y}}{d\boldsymbol{x}}$, we continue forward propagation using automatic differentation.

We compute the derivative of the eigenvalues with respect the the design variables using the left and right eigenvectors. Taking the partial derivative of the generalized eigenvalue problem with respect to an arbitrary design variable x yields:

$$\left(\frac{\partial A}{\partial x} - \frac{\partial \lambda_i}{\partial x} B - \Lambda_i \frac{\partial B}{\partial x}\right) U_i + (A - \lambda_i B) \frac{\partial U_i}{\partial x} = 0$$

where λ_i is an arbitrary eigenvalue and U_i is the corresponding right eigenvector. Premultiplying by the Hermitian transpose of the left-eigenvector V_i and rearranging yields an expression for the derivative of any eigenvalue with respect to any design variable:

$$\frac{\partial \lambda_i}{\partial x} = V_i^H \left(\frac{\partial A}{\partial x} - \lambda_i \frac{\partial B}{\partial x}\right) U_i / (V_i^T B U_i)$$

. We calculate both $\frac{\partial A}{\partial x}$ and $\frac{\partial B}{\partial x}$ using automatic differentiation. After solving for the derivative of the eigenvalues with respect to the design variables we continue forward propagation using automatic differentiation.

The main benefit of automatic differentiation compared to finite differencing is that automatic differentiation calculates exact rather than approximate derivatives. This allows optimizations to converge quicker and more reliably. In our case, automatic differentiation is also faster than finite differencing for computing sensitivities in most cases. The wall time required by each method in serial (using a 2.4 Ghz processor) and in parallel (using forty-five 2.4 Ghz processors) is shown in Table 7. Note that the overhead associated with data transfer reduces the speedup resulting from parallelizing the sensitivity calculations. This overhead can be reduced by reducing the number of constraints.

Table 7: Sensitivity Function Evaluation Wall Time

Case	Serial (s)	Parallel (s)
Forward Difference (without gusts)	349	40
Central Difference (without gusts)	844	168
Automatic Differentiation (without gusts)	149	19
Forward Difference (with gusts)	1858	175
Central Difference (with gusts)	3730	1711
Automatic Differentiation (with gusts)	1459	217

We verified all of our sensitivities using finite differencing. A directional derivative test of our sensitivities yielded a maximum discrepancy of 4.37×10^{-7} in the constraints and 2.974×10^{-10} in the objective function compared to forward finite differencing.

Optimization

We used SNOPT[41], a sequential quadratic programming (SQP) solver, to solve our optimization problem. The initial design variable values we passed to the optimizer are shown in Tables 8 and 9, though we found the optimized solution to not be very sensitive to the initial conditions. The aircraft generated using our initial design variable values violates several constraints, therefore we rely on the optimizer to find a feasible design for our optimization problem. The convergence history is shown in Fig. 8. A feasible design was found after 201 function evaluations and the optimal solution was found after 216 function evaluations.

Table 8: Initial Design Variables

Parameter	Value
Span (m)	42
Leading Edge Sweep (°)	15
Winglet Length (m)	2
Winglet Dihedral (°)	80
Skin Foam Thickness (mm)	5
Web Foam Thickness (mm)	1
Spar Location (x/c)	0.5
Design Velocity (m/s EAS)	8
Battery Mass at Station 3 (kg)	10
Battery Mass at Station 4 (kg)	10
Propeller Diameter (m)	2
Advance Ratio (V/nD)	0.91
Motor speed constant (rpm/V)	32
Motor No-Load Current (A)	1.6

Table 9: Initial Spanwise Varying Design Variables

Parameter	Station 1	Station 2	Station 3	Station 4	Station 5	Station 6
Chord (m)	2.0	1.4	1.4	1.4	1.4	0.5
Airfoil Thickness Ratio (t/c)	0.1	0.1	0.1	0.1	0.1	0.1
Twist (°)	4.0	6.0	4.0	2.0	0.0	−2.0
Spar Ply Thickness (mm)	1.0	1.0	1.0	1.0	1.0	1.0
Spar Width (w/c)	0.25	0.25	0.20	0.15	0.10	0.05

III. Results

Optimal Design

The optimized aircraft is shown in Fig. 9. Optimized design variables are presented in Tables 10 and 11. The aircraft has a wingspan of 63.33 m and an aspect ratio of 54.52. The mass breakdown of the aircraft is shown in Fig. 10.

The design relies on increased airfoil thickness ratios (relative to the original thickness of the E216 airfoil) and a narrow box beam to provide sufficient structural strength to prevent material failure, buckling, and flutter. At the wing root, the optimized spar thickness is equivalent to roughly 5 CFRP tape plies on either side of the spar's foam core. At the wing tip, the equivalent number of plies reduces to that of a single ply. There seems to be a slight preference for increased structural efficiency over aerodynamic efficiency, since airfoil thickness-to-chord ratios are up to 25 % thicker than the original thickness of the E216 airfoil (10.4 %), despite the greater lift-to-drag ratios of thinner airfoil sections.

Active inequality constraints at the end of the optimization consisted of energy balance, energy storage, stall, material failure, local buckling, and general stability constraints. Active energy balance and energy storage constraints indicate that using more efficient solar panels and higher specific energy batteries will reduce the mass of the optimized aircraft. Active stall constraints show that the optimizer has chosen to fly slowly (near stall speeds) to conserve energy. Flying at lower airspeeds reduces energy requirements since power is directly proportional to aircraft airspeed. Material failure constraints were active for the medium gust only, whereas buckling constraints were active at the cruise speed at a load factor of −1.0, at the dive speed at a load factor of 2.5, and at the flutter speed with a load factor of 1.0.

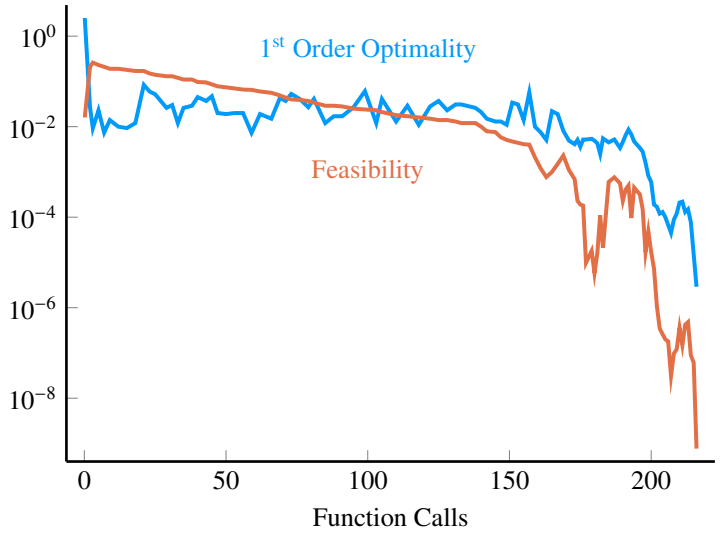

Figure 8: Optimization convergence history

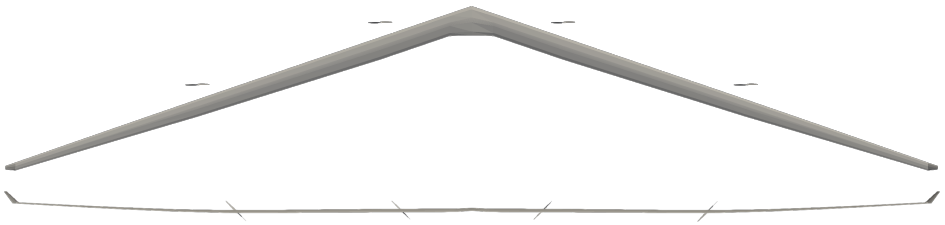

Figure 9: Top and rear view of the optimized aircraft during design operation.

Table 10: Optimized Design Variables

Parameter	Value
Span (m)	63.94
Leading Edge Sweep (°)	18.78
Winglet Length (m)	0.74
Winglet Dihedral (°)	36.39
Skin Foam Thickness (mm)	2.54
Web Foam Thickness (mm)	1.00
Spar Location (x/c)	0.47
Design Velocity (m/s EAS)	8.15
Battery Mass at Station 3 (kg)	31.50
Battery Mass at Station 4 (kg)	39.73
Propeller Diameter (m)	2.31
Advance Ratio (V/nD)	0.91
Motor speed constant (rpm/V)	32.0
Motor No-Load Current (A)	1.30

Table 11: Optimized Spanwise Varying Design Variables

Parameter	Station 1	Station 2	Station 3	Station 4	Station 5	Station 6
Chord (m)	2.0	1.52	1.52	1.16	0.52	0.24
Airfoil Thickness Ratio (t/c)	0.110	0.125	0.126	0.130	0.120	0.1
Twist (°)	2.28	7.05	6.84	5.44	3.40	−2.43
Spar Ply Thickness (mm)	0.53	0.53	0.37	0.37	0.1	0.1
Spar Width (w/c)	0.16	0.16	0.18	0.16	0.0	0.0

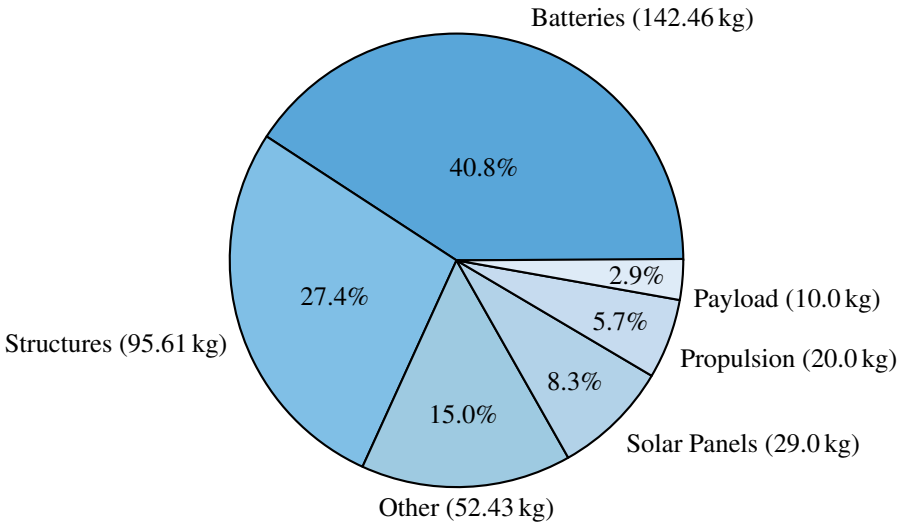

Figure 10: Mass distribution of the optimized design

The greater prevalence of stability constraints over material failure constraints suggests that the design is primarily stability constrained rather than material failure constrained.

Active bound constraints at the end of the optimization included root chord length, airfoil thickness-to-chord ratio at station 6, spar cap thicknesses at stations 5 and 6, web foam thickness, and motor speed constant. An active root chord length bound constraint simply indicates that removing the payload size constraint on the root chord would result in a lighter design. Active lower bound constraints for airfoil thickness-to-chord ratio and spar cap thicknesses indicate that the optimizer is removing structure towards the wingtips where loads are small. The active lower-bound constraint on motor speed constant indicates that motors with low speed constants are more appropriate for SR-HALE aircraft applications.

Deflection and aeroelastic twist (as predicted by ASWING) were small at the design operating airspeed as shown in Figs. 11 and 12. Some of the other operating points, however, exhibit non-negligible tip deflections. Small deflections at the design operating point can be attributed to the nature of swept flying wing configurations, whose lift distribution requires that wingtips are lightly loaded in order to obtain trimmed flight. For this aircraft, this lift distribution is achieved through a large amount of washout from the wing root to the wing tip and the aircraft's high taper ratio. This large amount of washout is likely also responsible for the large amount of deflection and aeroelastic twist that occur at low load factors.

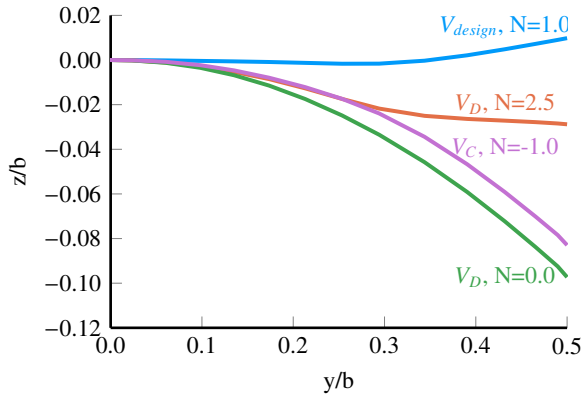

Figure 11: Wing deflection of optimized design

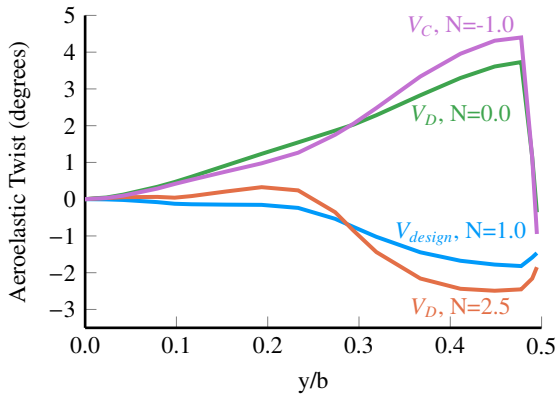

Figure 12: Aeroelastic twist of optimized design

We ran an additional optimization in which the thickness of the CFRP fabric in the skin was allowed to vary, with no lower bound on the thickness of the resulting value. Fabric ply thicknesses decreased from 0.1 mm to 0.053 mm. Total aircraft mass decreased from 349.5 kg to 294.2 kg. The results of this optimization suggest that a single ply of

CFRP fabric covering the aircraft skin provides more stiffness and strength than is necessary for achieving SR-HALE mission objectives. Better performance may therefore be obtained by either using a lighter material for the skin or by using a non-structural skin.

Parameter Sweeps

In order to calculate the sensitivity of the design to technology and mission requirement changes, we performed several parameter sweeps in which the optimal design was re-optimized while varying design altitude, design latitude limit, battery specific energy, solar panel system efficiency, avionics and payload power requirements, or minimum design velocity. The results of these parameter sweeps are presented in Figs. 13 to 18.

As seen in Fig. 13, decreases in design altitude allow lighter aircraft to be built. Increases in air density allow the aircraft to fly slower, reducing power requirements. Reduced power requirements then allow the aircraft's size to decrease because less solar panel area and battery mass are necessary for sustained flight. Airspace restrictions, may however, necessitate flying at higher altitudes, despite the benefits of flying at lower altitudes. Additionally, station keeping constraints may require that aircraft fly faster than would otherwise be optimal, which would reduce and/or eliminate the benefit of flying at lower altitudes.

Figure 14 shows that the optimized aircraft is very sensitive to design latitude limit choices at high latitudes, but less sensitive at lower latitudes. When the design latitude limit is reduced to 5°, the design is no longer constrained by energy balance constraints, in other words, the size of the aircraft is no longer constrained by solar capture requirements. The absence of active solar capture constraints, does not render the design insensitive to design latitude limit at latitudes below 10°, however, because further design latitude limit decreases decrease energy storage requirements because of shorter winter solstice night lengths at lower latitudes.

The design's sensitivity to battery specific energy is very high when battery specific energies are set to 350 Whr/kg, but becomes less sensitive at battery specific energies above 400 Whr/kg, as seen in Fig. 15. In part this is because less battery mass is required to store energy for night long flight when battery specific energy is increased for a given SR-HALE aircraft configuration. Reducing aircraft mass, however, can have a compounding effect which allows further decreases of aircraft mass in the optimized design. Reducing aircraft mass means that less lift is required to keep the aircraft aloft. This means that the aircraft can fly at lower design velocities than their larger counterparts. Flying at lower design velocities reduces total power requirements leading to smaller (and lighter) aircraft since the aircraft no longer requires as much solar panel area to capture sufficient energy for continuous operation. These smaller aircraft are less prone to structural instabilities and material failure and therefore can be designed with even less structure than their larger counterparts, further reducing aircraft mass. In essence, since decreasing aircraft mass reduces the impact of structural, stability, and solar capture constraints, increasing battery specific energy has the potential to greatly increase the performance of SR-HALE aircraft. However, as the influence of these constraints on the optimized aircraft's mass decreases, the impact of increasing battery specific energy on the total mass of the optimized aircraft also decreases as can be seen in Fig. 15.

Figure 16 shows that the design is sensitive to solar panel system efficiencies below 20 %, but not very sensitive at solar panel system efficiencies above 20 %. Considering the small increases in performance gained by increasing solar panel efficiency, it may be possible to reduce aircraft costs by using less solar panels and/or lower efficiency solar panels, however, since decreasing battery mass has a significant impact on the overall mass of the optimized aircraft a better course of action may be to incorporate a climb phase into the aircraft's mission in order to replace battery storage with potential energy storage. Incorporating a climb phase into the mission would likely cause the sensitivity of the optimization problem to solar panel efficiency (and possibly design latitude limit at low latitudes) to increase significantly.

We found the design to be very sensitive to avionics and payload power requirements for every set of power requirements we considered, as shown in Fig. 17. As power requirements increase, both additional battery mass and surface area are necessary to satisfy energy storage and capture constraints. Small changes in payload power requirements, may therefore cause large changes in the mass of optimal SR-HALE aircraft designs. So while the results of this study suggest that highly efficient solar panels may not be necessary, reducing payload power requirements seems to be an efficient way of enabling optimal designs with lower mass.

The last parameter sweep we performed was an investigation into the impact of minimum design velocities on optimal aircraft mass. The purpose of a minimum design velocity constraint is to ensure that aircraft can successfully station keep at the design altitude in the presence of persistent winds. As seen in Fig. 18, we found the design to be increasingly sensitive to increases in design velocity. Small increases in minimum design equivalent airspeed resulted in significant increases in aircraft mass. This significant increase in aircraft mass is due to the increased aircraft power and structural requirements caused by increasing design equivalent airspeed. As shown in Fig. 18, even a

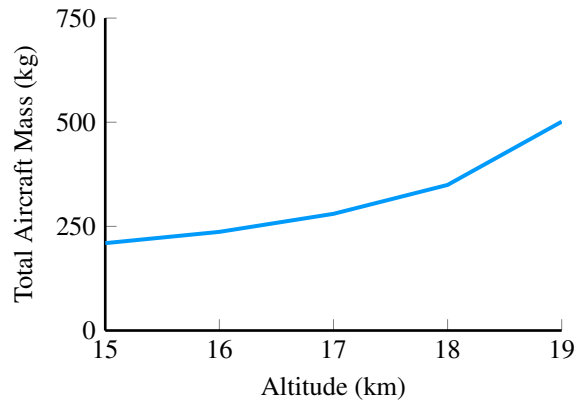

Figure 13: Sensitivity of optimized aircraft mass to design altitude

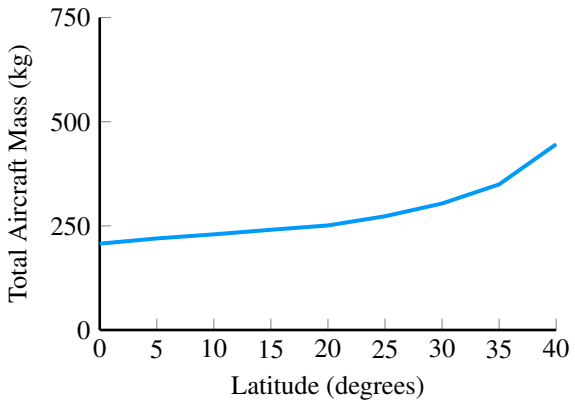

Figure 14: Sensitivity of optimized aircraft mass to design latitude limit

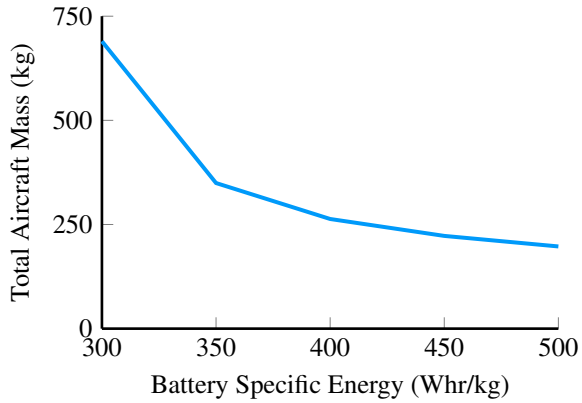

Figure 15: Sensitivity of optimized aircraft mass to battery specific energy

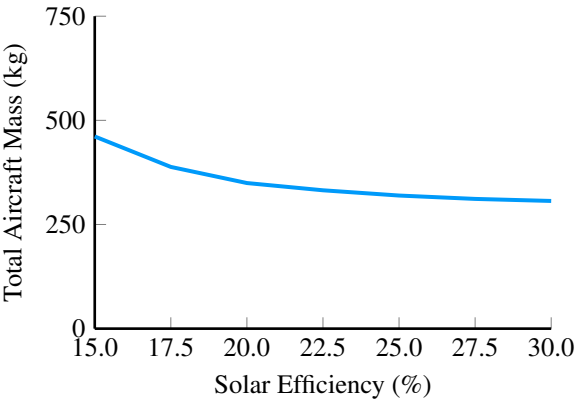

Figure 16: Sensitivity of optimized aircraft mass to total solar panel efficiency

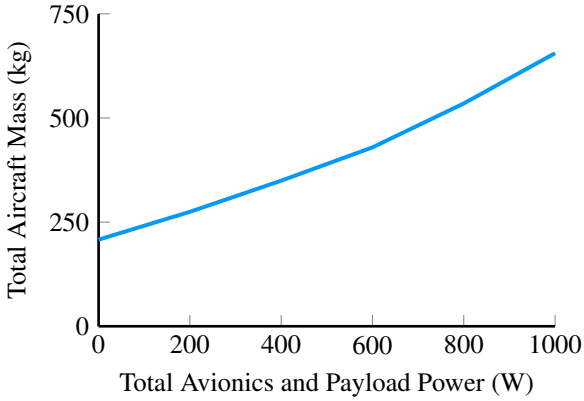

Figure 17: Sensitivity of optimized aircraft mass to combined avionics and payload power requirements

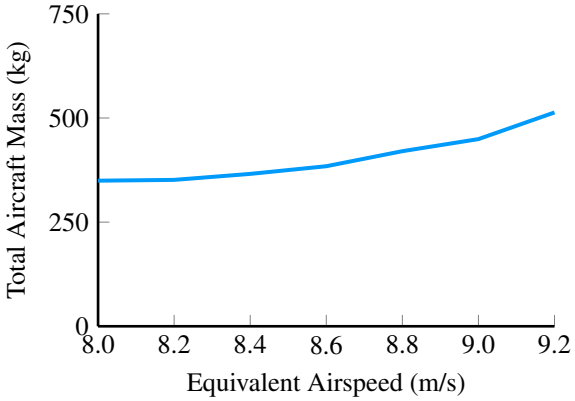

Figure 18: Sensitivity of optimized aircraft mass to minimum design velocity

relatively modest increase in minimum design equivalent airspeed may cause a large increase in optimal aircraft mass. Specifically a 1.2 m/s increase in minimum equivalent airspeed from 8.0 m/s to 9.2 m/s resulted in an aircraft design mass increase of 163.8 kg.

IV. Conclusions

In this paper we presented an SR-HALE aircraft optimization framework which models and constrains the nonlinear aeroelasticity of flexible aircraft while remaining suitable for use with gradient-based optimization. We incorporated nonlinear aeroelasticity into the optimization framework by using the existing flexible aircraft analysis tool ASWING, and constructed energy capture, energy storage, material failure, local buckling, stall, longitudinal stability, and coupled flight and aeroelastic mode stability constraints that are suitable for use with gradient-based optimization. We then used this framework to minimize the mass of a flying wing SR-HALE aircraft defined by six spanwise stations subject to structural constraints based on transport category aircraft design requirements. We also ensured that the final design was conservative through mass and drag markups.

The optimized aircraft's aspect ratio and surface area were 54.52 m^2 and 73.56 m^2 respectively and the aircraft's mass was 349.5 kg. Despite the high aspect ratio design, the aircraft exhibited very little aeroelastic deflection and twist at the design airspeed, due to the trim requirements of swept flying wing aircraft. Sufficient structural strength was provided to the design through varying airfoil thicknesses, spar widths and thicknesses, and chord lengths. The optimized design featured airfoil thickness over chord ratios as large as 0.13 and a spar cap with the equivalent thickness of up to approximately 5 plies of unidirectional CFRP on either side of a foam core. We used CFRP fabric for the skin of our aircraft, but found that better performance may be obtained by either using a lighter material for the skin, or by using a non-structural skin.

Finally, we performed several parameter sweeps to determine the sensitivity of optimized SR-HALE aircraft designs to various mission requirements and technological capabilities. Investigated parameters include design altitude, design latitude, battery specific energy, solar panel system efficiency, combined avionics and payload power requirements, and minimum design velocities. We found the sensitivity of the design to all of these parameters to be high, except at higher solar panel system efficiencies and low latitudes. Incorporating a climb phase into the mission profile of our SR-HALE aircraft to store potential energy, however, would likely cause the sensitivity of the optimized design to these parameters to increase by reducing the amount of batteries the aircraft must carry to power night-long flight.

Future work includes investigating the applicability of the design features and trends found within this paper to other configurations and modeling the impact of active aeroelastic control on the design of SR-HALE aircraft. Work also needs to be done to investigate how optimal SR-HALE aircraft designs change when coupled with trajectory optimizations. Future SR-HALE aircraft optimizations would also benefit from improved methods of modeling and constraining coupled flight and aerostructural modes appropriate for gradient-based optimization. A major limitation of the current approach is that it applies an equivalent constraint to all flight and aeroelastic modes. In practical design, it may be advisable to apply different safety factors to different modes and/or allow certain aeroelastic modes to be controlled through active aeroelastic control.

Acknowledgments

We gratefully acknowledge support from The Connectivity Lab at Facebook and the Utah NASA Space Grant Consortium. Design choices, findings, and conclusions are those of the authors and do not necessarily reflect the views of Facebook. We also gratefully acknowledge Kevin Moore for his aid with the propulsion models used in this paper and Nathaniel Gates for providing propeller non-dimensional properties from coupled propulsion and trajectory SR-HALE aircraft optimizations.

References

[1] Boucher, R. J., "Sunrise, the world's first solar-powered airplane," *Journal of Aircraft*, Vol. 22, No. 10, 1985, pp. 840–846. , http://dx.doi.org/10.2514/3.45213.

[2] Karapantazis, S., and Pavlidou, F.-N., "Broadband Communications via High-Altitude Platforms: A Survey," *IEEE Communications Surveys & Tutorials*, Vol. 7, No. 1, 2005, pp. 2–31. , https://doi.org/10.1109/COMST.2005.1423332.

[3] Cestino, E., "Design of solar high altitude long endurance aircraft for multi payload & operations," *Aerospace Science and Technology*, Vol. 10, No. 6, 2006, pp. 541–550. , https://doi.org/10.1016/j.ast.2006.06.001.

[4] Baldock, N., and Mokhtarzadeh-Dehghan, M., "A study of solar-powered, high-altitude unmanned aerial vehicles," *Aircraft Engineering and Aerospace Technology*, Vol. 78, No. 3, 2006, pp. 187–193. , https://doi.org/10.1108/17488840610663648.

[5] Nickol, C., Guynn, M., Kohout, L., and Ozoroski, T., "High Altitude Long Endurance Air Vehicle Analysis of Alternatives and Technology Requirements Development," *Aerospace Sciences Meetings*, American Institute of Aeronautics and Astronautics, 2007. , https://doi.org/10.2514/6.2007-1050.

[6] Burton, M., and Hoburg, W., "Solar and Gas Powered Long-Endurance Unmanned Aircraft Sizing via Geometric Programming," *Journal of Aircraft*, Vol. 55, No. 1, 2017, pp. 212–225. , https://doi.org/10.2514/1.C034405.

[7] Burton, M. J., Drela, M., Courtin, C., Colas, D., Suryakumar, V. S., and Roberts, N. H., "Solar Aircraft Design Trade Studies Using Geometric Programming," *2018 Multidisciplinary Analysis and Optimization Conference*, American Institute of Aeronautics and Astronautics, 2018. , https://doi.org/10.2514/6.2018-3740.

[8] Colas, D., Roberts, N. H., and Suryakumar, V. S., "HALE Multidisciplinary Design Optimization Part I: Solar-Powered Single and Multiple-Boom Aircraft," *2018 Aviation Technology, Integration, and Operations Conference*, American Institute of Aeronautics and Astronautics, 2018. , https://doi.org/10.2514/6.2018-3028.

[9] Colas, D., Roberts, N. H., and Suryakumar, V. S., "HALE Multidisciplinary Design Optimization Part II: Solar-Powered Flying-Wing Aircraft," *2018 Aviation Technology, Integration, and Operations Conference*, American Institute of Aeronautics and Astronautics, 2018. , https://doi.org/10.2514/6.2018-3029.

[10] Drela, M., "Integrated simulation model for preliminary aerodynamic, structural, and control-law design of aircraft," *40th Structures, Structural Dynamics, and Materials Conference and Exhibit*, American Institute of Aeronautics and Astronautics, 1999. , https://doi.org/10.2514/6.1999-1394.

[11] Patil, M., and Taylor, D., "Gust Response of Highly Flexible Aircraft," *47th AIAA/ASME/ASCE/AHS/ASC Structures, Structural Dynamics, and Materials Conference*, American Institute of Aeronautics and Astronautics, 2006. , https://doi.org/10.2514/6.2006-1638.

[12] Patil, M., "Nonlinear Gust Response of Highly Flexible Aircraft," *48th AIAA/ASME/ASCE/AHS/ASC Structures, Structural Dynamics, and Materials Conference*, American Institute of Aeronautics and Astronautics, 2007. , https://doi.org/10.2514/6.2007-2103.

[13] Shearer, C. M., and Cesnik, C. E. S., "Nonlinear Flight Dynamics of Very Flexible Aircraft," *Journal of Aircraft*, Vol. 44, No. 5, 2007, pp. 1528–1545. , https://doi.org/10.2514/1.27606.

[14] Su, W., and Cesnik, C. E. S., "Nonlinear Aeroelasticity of a Very Flexible Blended-Wing-Body Aircraft," *Journal of Aircraft*, Vol. 47, No. 5, 2010, pp. 1539–1553. , https://doi.org/10.2514/1.47317.

[15] Mardanpour, P., Hodges, D. H., Neuhart, R., and Graybeal, N., "Engine Placement Effect on Nonlinear Trim and Stability of Flying Wing Aircraft," *Journal of Aircraft*, Vol. 50, No. 6, 2013, pp. 1716–1725. , https://doi.org/10.2514/1.C031955.

[16] Mardanpour, P., Richards, P. W., Nabipour, O., and Hodges, D. H., "Effect of multiple engine placement on aeroelastic trim and stability of flying wing aircraft," *Journal of Fluids and Structures*, Vol. 44, 2014, pp. 67 – 86. , https://doi.org/10.1016/j.jfluidstructs.2013.09.018.

[17] Cesnik, C. E., Palacios, R., and Reichenbach, E. Y., "Reexamined Structural Design Procedures for Very Flexible Aircraft," *Journal of Aircraft*, Vol. 51, No. 5, 2014, pp. 1580–1591. , https://doi.org/10.2514/1.C032464.

[18] Gavan, J., Tapuchi, S., and Grace, D., "Concepts and main applications of high-altitude-platform radio relays," *URSI Radio Science Bulletin*, Vol. 2009, No. 330, 2009, pp. 20–31. , https://doi.org/10.23919/URSIRSB.2009.7909716.

[19] Center for International Earth Science Information Network (CIESIN)–Columbia University, "Gridded Population of the World, Version 4 (GPWv4): Population Density," , 2016. , https://doi.org/10.7927/H4X63JVC.

[20] McDonnell, T. G., Mehr, J. A., and Ning, A., "Multidisciplinary Design Optimization Analysis of Flexible Solar-Regenerative High-Altitude Long-Endurance Aircraft," *2018 AIAA/ASCE/AHS/ASC Structures, Structural Dynamics, and Materials Conference*, American Institute of Aeronautics and Astronautics, 2018. , https://doi.org/10.2514/6.2018-0107.

[21] Kassapoglou, C., *Good Design Practices and Design Rules of Thumb*, chapter and pages, pp. 343–349. , https://doi.org/10.1002/9781118536933.ch12.

[22] Drela, M., "XFOIL: An Analysis and Design System for Low Reynolds Number Airfoils," *Low Reynolds Number Aerodynamics*, edited by T. J. Mueller, Springer Berlin Heidelberg, Berlin, Heidelberg, 1989, pp. 1–12. , https://doi.org/10.1007/978-3-642-84010-4_1.

[23] Gates, N. S., Moore, K. R., Ning, A., and Hedengren, J. D., "Combined Trajectory, Propulsion, and Battery Mass Optimization for Solar-Regenerative High-Altitude Long Endurance Unmanned Aircraft," *AIAA Scitech 2019 Forum*, American Institute of Aeronautics and Astronautics, San Diego, CA, 2019. , https://doi.org/10.2514/6.2019-1221.

[24] Drela, M., "QProp Propeller/Windmill Analysis and Design," Massachusets Inst. of Technology, Cambridge, MA, 2007. http://web.mit.edu/drela/Public/web/qprop/motor1_theory.pdf.

[25] Moore, K. R., and Ning, A., "Distributed Electric Propulsion Effects on Existing Aircraft Through Multidisciplinary Optimization," *2018 AIAA/ASCE/AHS/ASC Structures, Structural Dynamics, and Materials Conference*, American Institute of Aeronautics and Astronautics, 2018. , https://doi.org/10.2514/6.2018-1652.

[26] Gueymard, C., *SMARTS2, A Simple Model of the Atmospheric Radiative Transfer of Sunshine: Algorithms and performance assessment*, Florida Solar Energy Center, 1995.

[27] Kreisselmeier, G., and Steinhauser, R., "Systematic Control Design by Optimizing a Vector Performance Index," *IFAC Proceedings Volumes*, Vol. 12, No. 7, 1979, pp. 113–117. , https://doi.org/10.1016/S1474-6670(17)65584-8.

[28] Bir, G. S., *User's guide to PreComp (Pre-Processor for Computing Composite Blade Properties)*, National Renewable Energy Laboratory, Golden, CO, 2006. , https://doi.org/10.2172/876556.

[29] Revels, J., Lubin, M., and Papamarkou, T., "Forward-Mode Automatic Differentiation in Julia," *Computing Research Repository*, 2016. http://arxiv.org/abs/1607.07892.

[30] Sale, D., Aliseda, A., and Motley, M., "Structural Optimization of Composite Blades for Wind and Hydrokinetic Turbines," *Proceedings of the 1st Marine Energy Technology Symposium*, Washington, D.C., 2013. http://marineenergytechnologysymposium.org/download/2013/Structural-Optimization-of-Composite-Blades-for-Wind-and-Hydrokinetic-Turbines.pdf.

[31] Tsai, S. W., and Wu, E. M., "A General Theory of Strength for Anisotropic Materials," *Journal of Composite Materials*, Vol. 5, No. 1, 1971, pp. 58–80. , https://doi.org/10.1177/002199837100500106.

[32] Tomblin, J., Sherraden, J., Seneviratne, W., and Raju, K., "Advanced General Aviation Transport Experiments. A-Basis and B-Basis Design Allowables for Epoxy-Based Prepreg Toray T700GC-12K-31E/#2510 Unidirectional Tape," , 2002. ps://www.niar.wichita.edu/agate/Documents/Materials/WP3.3-033051-132.pdf.

[33] Tomblin, J., Sherraden, J., Seneviratne, W., and Raju, K., "Advanced General Aviation Transport Experiments. ABasis and BBasis Design Allowables for EpoxyBased Prepreg: TORAY T700SC-12K-50C/#2510 Plain Weave Fabric," , 2002. ttps://www.niar.wichita.edu/agate/documents/materials/wp3.3-033051-134.pdf.

[34] Whitehead, R. S., "Lessons learned for composite structures," *The First NASA Advanced Composites Technology Conference, Part 1*, NASA Langley Research Center, 1991, pp. 399–415. https://ntrs.nasa.gov/search.jsp?R=19930021255.

[35] Johnson, A., "6 - Structural component design techniques," *Handbook of Polymer Composites for Engineers*, edited by L. Hollaway, Woodhead Publishing Series in Composites Science and Engineering, Woodhead Publishing, 1994, pp. 136 – 180. , https://doi.org/10.1533/9781845698607.136.

[36] Tarján, G., Sapkás, A., and Kollár, L. P., "Local buckling of composite beams," *17th International Conference on Composite Materials, ICCM-17*, 2009. http://iccm-central.org/Proceedings/ICCM17proceedings/papers/IF22.6%20Kollar.pdf.

[37] Poon, N. M. K., and Martins, J. R. R. A., "An adaptive approach to constraint aggregation using adjoint sensitivity analysis," *Structural and Multidisciplinary Optimization*, Vol. 34, No. 1, 2007, pp. 61–73. https://doi.org/10.1007/s00158-006-0061-7.

[38] Morgado, J., Vizinho, R., Silvestre, M. A. R., and Pscoa, J. C., "XFOIL vs CFD performance predictions for high lift low Reynolds number airfoils," *Aerospace Science and Technology*, Vol. 52, 2016, pp. 207–214. https://doi.org/10.1016/j.ast.2016.02.031.

[39] Wang, L., Liu, X., Guo, L., Renevier, N., and Stables, M., "A mathematical model for calculating cross-sectional properties of modern wind turbine composite blades," *Renewable Energy*, Vol. 64, 2014, pp. 52–60. https://doi.org/10.1016/j.renene.2013.10.046.

[40] Kollár, L. P., and Springer, G. S., *Mechanics of Composite Structures*, Cambridge University Press, 2003. .

[41] Gill, P. E., Murray, W., and Saunders, M. A., "SNOPT: An SQP algorithm for large-scale constrained optimization," *Society for Industrial and Applied Mathematics Review*, Vol. 47, No. 1, 2005, pp. 99–131. , https://doi.org/10.1137/S0036144504446096.